Supplementary Information

Specific biomolecule corona is associated with ring-shaped organization of silver nanoparticles in cells

Daniela Drescher, Peter Guttmann, Tina Büchner, Stephan Werner, Gregor Laube, Andrea Hornemann, Basel Tarek, Gerd Schneider, and Janina Kneipp

I. METHODS

Particle characterization: The hydrodynamic diameter and zeta-potential of suspended Ag nanoparticles were examined using a Zetasizer Nano ZS (Malvern Instruments, *United Kingdom*) operating at a wavelength of 633 nm, a laser power of 4 mW and a scattering angle of 173˚. The methods of CONTIN and NNLS (Non Negative Least Squares algorithm), as implemented in the Malvern software, were used for fitting of the DLS correlation. For determination of the particle size from DLS data the intensity-weighted size distribution was utilized. The viscosity of the samples was determined with an AMVn viscometer (Anton Paar, *Austria*). Extinction spectra were recorded with a UV-vis/NIR double-beam spectrophotometer (JASCO GmbH, *Germany*). Transmission electron micrographic images of silver nanoparticles were obtained with a Tecnai G^2 20 S-TWIN microscope (FEI, Hillsboro, USA) using an acceleration voltage of 200 kV.

TEM preparation*:* For electron microscopy, 3T3 cells were treated under the same experimental conditions as for the viability tests. After a 3h-exposure to Ag nanoparticles (50 pM) suspended in DMEM with 10 % FCS, the cells were washed twice with PBS and fixed with 2.5% glutaraldehyde in PBS (pH 7.4) for 15 min. After several washes with PBS, the cells were postfixed in 1 % osmium tetroxide in 0.1 M phosphate buffer (PB, pH 7.4) for 10 min and washed repeatedly in PB. Subsequently, the cells were dehydrated in a graded series of ethanol, including a block staining with 2 % uranyl acetate in 70 % ethanol. Hydroxypropyl methacrylate (HPMA, Fluka, *Switzerland*) was used as intermedium to transfer the specimens to Epon 812 resin. Resin infiltration and polymerization was carried out in cell culture multiwell plates. Ultrathin sections (70 nm) of aldehyde-fixed and in Epon 812 resin embedded cells were stained with uranyl acetate and lead citrate and were examined with a Zeiss EM 900 electron microscope at 80 kV (Carl Zeiss SMT GmbH, *Germany*). Electron micrographs were recorded using a 1K slow-scan CCD camera (Proscan).

Cell viability test (XTT assay): Cytotoxicity of silver nanoparticles was evaluated utilizing XTT reagent (2,3-bis-(2-methoxy-4-nitro-5-sulfophenyl)-2H-tetrazolium-5-carboxanilide in a procedure described recently[1].

II. Additional Data and Information

Transmitted intensity and linear absorption coefficient

The contrast in X-ray microscopic images of vitrified cells is based on the stronger absorption of soft X-rays in organic matter as compared to vitreous ice in the so-called water window from 280 to 530 eV photon energy (between the K-absorption edge of carbon and the K-absorption edge of oxygen).[2, 3] For a narrow beam of mono-energetic photons with the initial intensity $\mathbf{I_0}$, the intensity of photons transmitted **I** across the distance **x** in a material with the linear absorption coefficient (LAC) **μ** can be expressed as:

$$(1) \qquad I = I_0 e^{-\mu x} \quad .$$

The LAC for each volume element of a sample is given by the voxels obtained in the tomographic reconstruction, for example in Figure 2 of the manuscript text. In contrast, the projection image (for example, Figures 1 in the manuscript or Figure S3) is the *sum* of the absorption coefficients of all molecules along the optical path. The penetration depth of X-rays varies for different materials[4] (LAC is dependent on the density of a material) as illustrated in Figure S1.

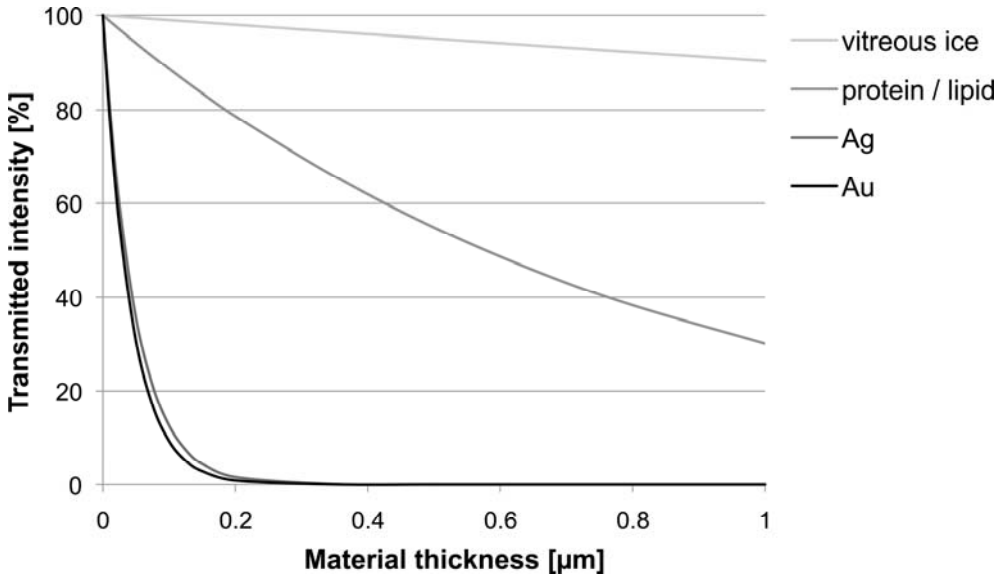

Figure S1. Relative transmitted intensity at photon energy of 510 eV as a function of material thickness for vitreous ice, model protein/lipid, silver and gold based on the material's linear absorption coefficient: 0.1, 1.2, 20.7 and 23.7 μm^{-1},[2, 4] respectively.

Here, the transmitted intensity at photon energy of 510 eV is shown for vitreous ice, protein / lipids, silver and gold as function of the material thickness. The linear absorption coefficients of silver (20.7 μm^{-1}) and gold (23.7 μm^{-1}) are high compared to vitreous ice (0.1 μm^{-1}) and a model protein/lipid (~1.2 μm^{-1}).[2, 4] Since the densities of biological structures are often unknown, we use here the LAC of a model protein/lipid.[2] A silver layer with a thickness of 50 nm reduces the intensity of 510 eV energy already to 36 %, while the intensity is not attenuated for vitreous ice (100 %) and marginal for proteins/lipids (94 %) of the same thickness. At photon energy of 510 eV employed in our investigations, vitreous ice is bright while organic structures such as lipid membranes, nucleolus and proteins are visible as grey shades. Due to different molecule compositions and densities, cellular organelles differ in contrast.[5-7] Owing to their high density, silver and gold appear dark as illustrated in Figure S2 by simulation of the image contrast.

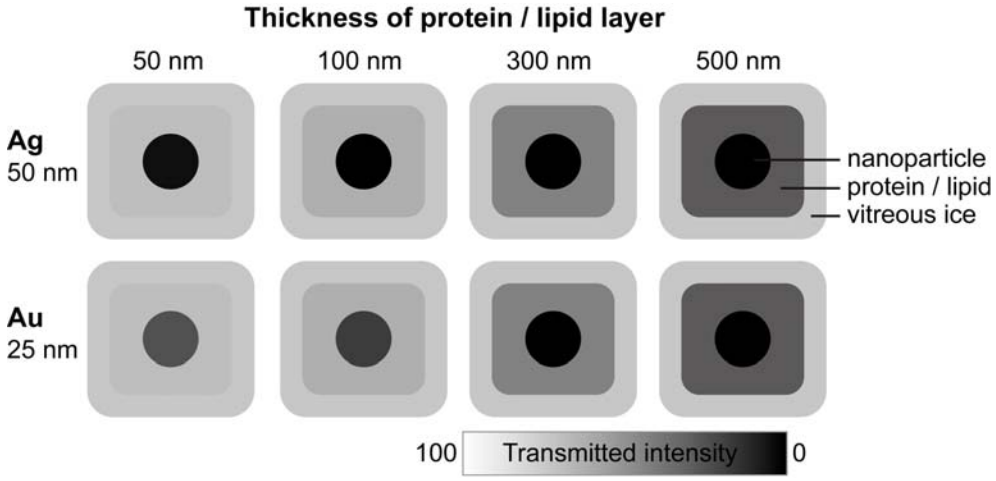

Figure S2. Simulation of the image contrast in X-ray microscopy for silver and gold nanoparticles sized 50 nm and 25 nm, respectively, surrounded by proteins/lipids in vitreous ice (outermost layer, thickness 3 µm). The contrast is illustrated for different thickness of proteins/lipids along the optical path.

Computed X-ray microscopy based on the projection images can be utilized to reconstruct the local LAC for each voxel in the 3D volume. This enables the determination of nanoparticle size and quantification of particle aggregates since the grey shades are quantitative. The analysis of image contrast in the X-ray microscopic images was used for example by Kapishnikov *et al.* to evaluate the lipid thickness around hemozoin crystals in infected red blood cells.[5]

Due to the significant difference in LAC, silver nanoparticles with a diameter of 50 nm and gold nanoparticles with a diameter of 25 nm can be clearly distinguished from the biological matrix as observed in our X-ray microscopic images (see also simulated image contrast in Figure S2). The high penetration depth of soft X-rays in vitreous ice allows the investigation of silver nanoparticle distribution in whole vitrified mammalian cells of up to 10 µm thickness so that fixation, staining and sectioning of the cells are not required.

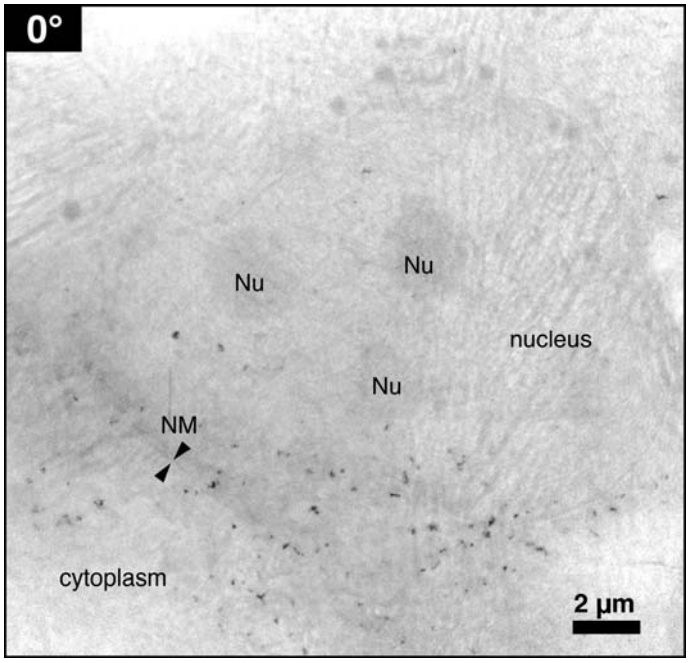

Movie S1. (please see additional file) X-ray microscopic tilt series of an individual fibroblast cell incubated with silver nanoparticles for 24 hours (see movie in the supplementary). Here, the corresponding projection image at 0° is shown. Ice structures above and below the tomography grid are visible as freezing artifacts in the microscopic images. Abbreviation: Nu, nucleolus; NM, nuclear membrane. Single silver nanoparticles and particle aggregates are visible as black spots.

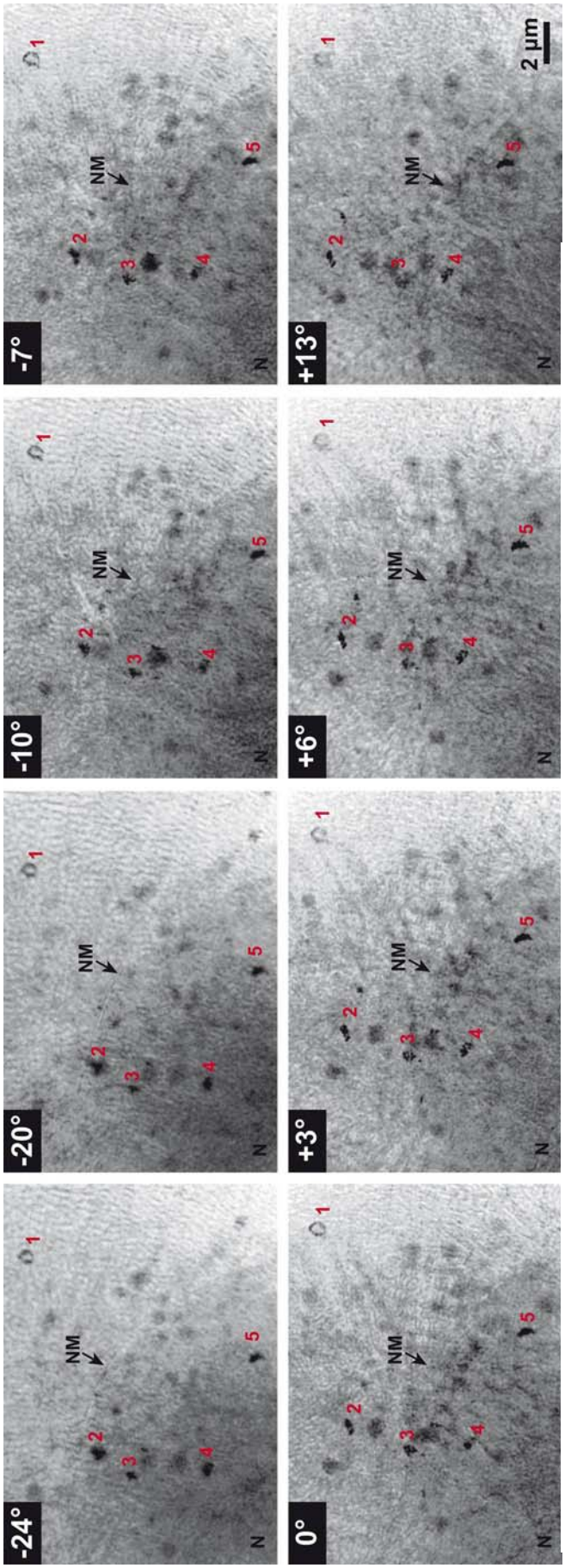

Figure S3. X-ray microscopic images at different tilt angles of an individual 3T3 fibroblast cell incubated with silver nanoparticles for 24 hours. Abbreviation: NM, nuclear membrane; N, nucleus; 1 silver nanoring, 2-5 silver nanoparticle aggregates.

Toxicity of silver nanoparticles

To assess the toxicity of the nanoparticles, the XTT assay was applied to test the metabolic activity after a 24-hour exposure to different amounts of nanoparticles and their aggregates (Figure S4). While concentrations of up to 10 pM citrate-reduced silver nanoparticles (corresponding to 5.5 µg/ml silver) in the cell culture medium do not show cytotoxic effects, the cell viability is significantly reduced to about 65 % at a nanoparticle concentration of 100 pM (55 µg/ml silver). This is in accordance with previous studies on the cytotoxicity of silver nanoparticles.[8, 9] As illustrated by the comparison of results obtained with silver nanoparticles of the same concentration that had been aggregated in the presence of 150 mM sodium chloride before adding them to the culture medium (Figure S4), cytotoxicity strongly depends on the agglomeration state of the particles. Pre-aggregated silver nanoparticles only exert a marginal effect on the cell viability, even at high concentrations (Figure S4). Similar results from earlier experiments where we used other types of toxic nanoparticles,[1] indicated that aggregates of nanoparticles were less likely to be internalized by the cells.

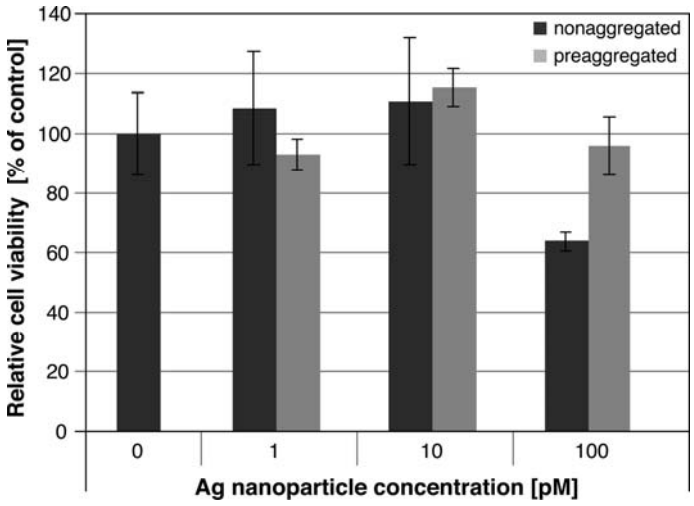

Figure S4. Viability of 3T3 cells after 24h-exposure to varying concentrations of citrate-stabilized silver nanoparticles dispersed in cell culture medium as determined by XTT assay. Particles were used as-synthesized or preaggregated with 150 mM sodium chloride.

X-ray microscopy and SERS experiments with gold nanoparticles

To investigate the influence of the surface chemistry of the nanoparticles on their intracellular organization, cryo X-ray nanotomography and surface-enhanced Raman scattering (SERS) were used to study gold nanoparticle distribution in the cell ultrastructure and to characterize the nanoparticle surface inside the cell, respectively.

The X-ray microscopic images (Figure S5) of individual fibroblast cells exposed to gold nanoparticles for 3 and 24 hours show a high amount of intracellular nanoparticles. Similar to the observations made for the silver nanoparticles (see manuscript text), the gold particles are visible due to the high linear absorption coefficient of gold as compared to organic matter and vitreous ice (see Figure S1 and S2). After 3 hours of incubation (Figure S5A), single nanoparticles and small aggregates are localized in the peri-nuclear region of the fibroblast cell. With increasing incubation time (Figure S5B), more particle aggregates are formed inside the cell due to multivesicular fusion. In contrast to silver nanoparticles inside the fibroblast cells, X-ray microscopic tilt series of cells incubated with gold nanoparticles do *not* provide evidence of 2-dimensional ring-shaped organization.

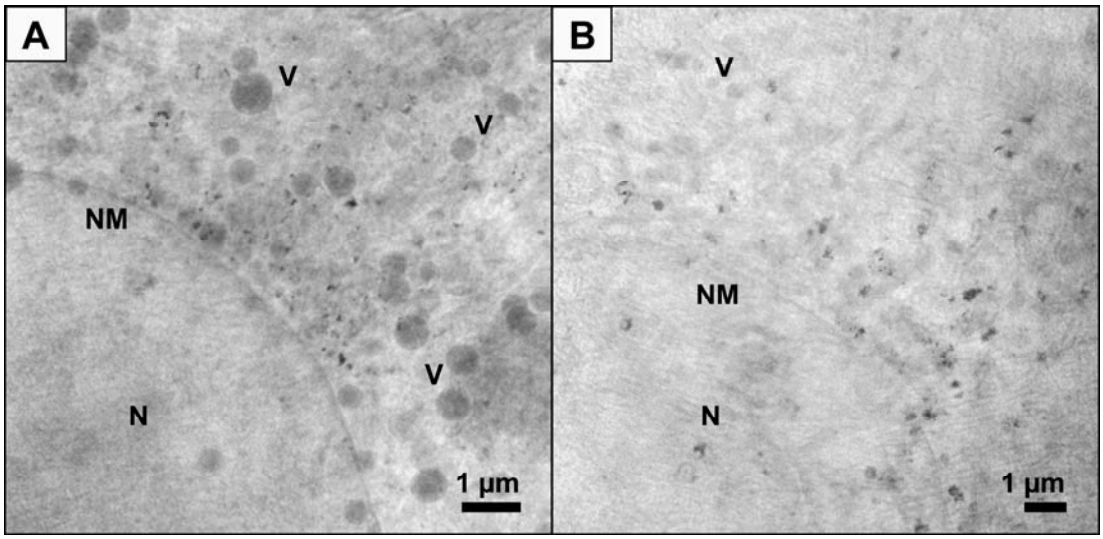

Figure S5. X-ray microscopic images of individual fibroblast cells incubated with gold nanoparticles for 3 hours (**A**) and 24 hours (**B**). Abbreviations: N, nucleus; NM, nuclear membrane; V, vesicle. Single gold nanoparticles and particle aggregates are visible as black spots in the biomatrix.

The different intracellular organization could be explained by different surface properties of gold and silver nanoparticles, leading to different nanoparticle surface composition. SERS [10-12] not only with silver but also with gold nanoparticles has been made use of in a number of biomedical applications.[13-19] We can also study the molecules at the gold nanoparticle surface inside the cells by SERS. The SERS signals obtained from cells containing gold nanoparticles

provide evidence of many different types of molecules present in the immediate endosomal environment surrounding the nanoparticles. As we have described in earlier work[20-22], the bands in these spectra can be assigned to protein / amino acid components, nucleotides, carbohydrates, and lipid constituents. The spectra displayed in Figure S6A differ in absolute intensity and in the number of bands depending on the particle incubation time (compare grey and black spectra). This is in accord with earlier observations, where differences in the SERS data were found as a consequence of changed chemical composition during endosomal maturation and also of altered plasmonic properties due to particle accumulation and aggregate formation.[21]

To compare the spectra obtained from gold nanoparticles inside the cells with those measured when particles were suspended in cell culture medium, fetal calf serum (FCS), Dulbecco's modified eagle medium (DMEM), and cysteine were examined as reference solutions (Figure S6B). The FCS spectrum obtained with gold nanoparticles is dominated by the C-S stretching vibration at 665 cm^{-1} of cysteine as constituent of the proteins similar to the spectrum measured with the silver nanoparticles (compare with manuscript Figure 3).

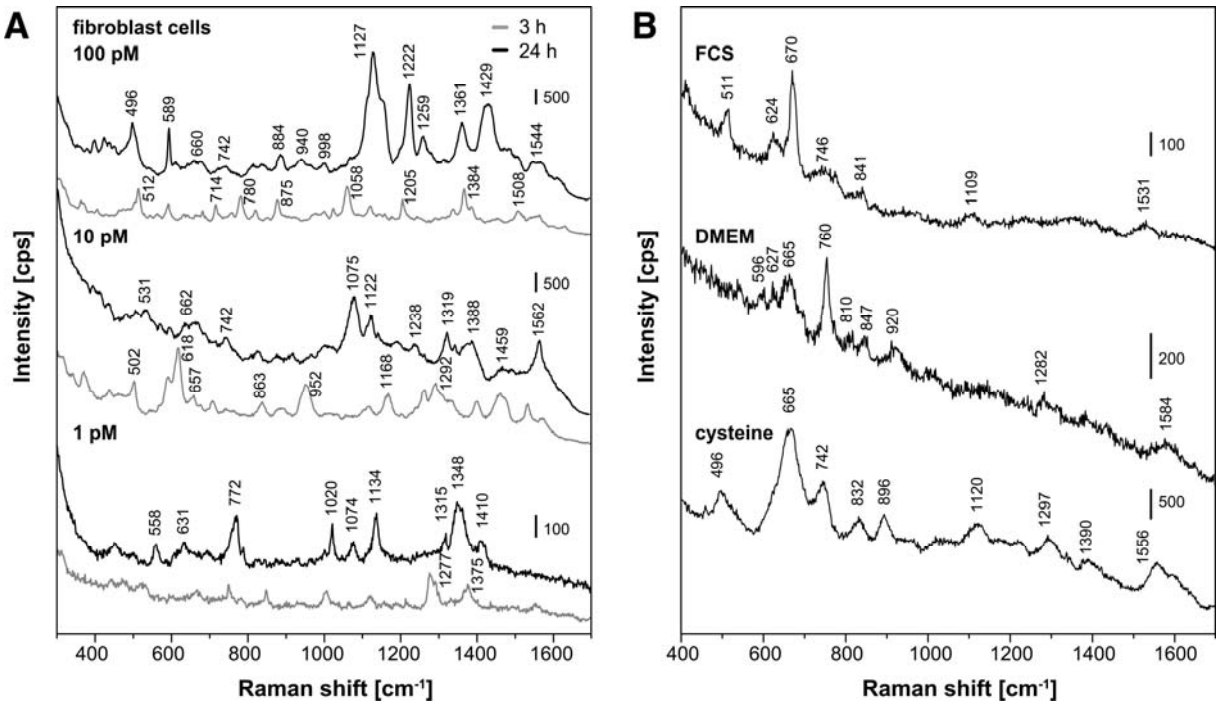

Figure S6. Representative SERS spectra of 3T3 fibroblast cells (**A**) and of cell culture relevant media (**B**) incubated with citrate-stabilized gold nanoparticles. Cells were exposed to gold nanoparticles at three different concentrations in cell culture medium for 3 hours (gray traces) and 24 hours (black traces). Excitation wavelength 785 nm; acquisition time 1s; laser intensity for (**A**) $8 \cdot 10^4$ W/cm^2 and for (**B**) $3 \cdot 10^6$ W/cm^2. Abbreviations: FCS, fetal calf serum; DMEM, Dulbecco's modified eagle medium.

The Raman band at 511 cm^{-1} (FCS spectrum, Figure S6B) can be assigned to the S-S stretching vibration of proteins which is not obvious in the SERS spectra of silver nanoparticles (Figure 3), where Ag-S bonds are formed. The SERS spectrum of DMEM shows many spectral features typical for amino acids, e.g., C-S stretching vibration at 665 cm^{-1}, indol symmetric breathing of tryptophan at 760 cm^{-1} and C-COO^- stretching vibration at 920 cm^{-1}. Raman spectrum of gold nanoparticles suspended in L-cysteine is similar to that in FCS solution (Figure S6B), e.g., C-S stretching vibration at 665 and 742 cm^{-1} and the C-N stretching vibration at 1120 cm^{-1}.

In contrast to silver nanoparticles, the SERS spectra of gold nanoparticles inside the cells are not dominated by Raman signals of components of the cell culture medium. The varying SERS signature of gold nanoparticles in fibroblast cells suggests a variable surface composition over the timescale of these experiments.

Size, plasmonic properties, and stability of silver and gold nanoparticles

In order to evaluate the stability of silver nanoparticles in the media relevant for the cell experiments, the size distribution and plasmonic properties were determined by dynamic light scattering (DLS) and UV-vis measurements. The hydrodynamic diameter of silver nanoparticles suspended in cell culture media was determined based on the intensity-weighted particle size distribution (Figure S7A). As-prepared citrate-stabilized silver nanoparticles show a bimodal distribution of hydrodynamic diameter with maxima at 10 nm and 50 nm (Figure S7A, solid line), in accordance with the high degree of polydispersity observed in transmission electron microscopy (TEM, inset in Figure S7A). The TEM image in Figure S7A gives a particle size of 50 ± 20 nm and on the majority a spherical particle morphology.

Independent of a decrease of the nanoparticle zeta potential from -35 mV in water to -11 mV, the nanoparticles are stabilized in the presence of an excess of FCS in the culture medium, that is, under standard incubation conditions (10 % FCS in DMEM). The mean hydrodynamic diameter was increased by about 20 nm, which is an indicator for the adsorption of proteins and / or other molecules (Figure S7A, gray line). The extinction spectrum shows a red-shift of 8 nm and slight broadening of the plasmon band (Figure S7B, gray line). We attribute these effects to adsorption of serum proteins at the particle surface and stabilization of the nanoparticles by steric repulsion. In PBS and DMEM containing salt at physiologic concentrations and no serum proteins, the mean particle size increases to about 100 nm as a result of electrostatic destabilization (zeta-potential is reduced from -35 mV in water to -23 mV in DMEM) that results in aggregation of the particles (Figure S7A, dashed and dotted lines). Aggregation of silver nanoparticles is also evidenced in the extinction spectra showing an extended plasmon band (Figure S7B). Similar effects regarding particle stabilization and aggregation can be observed in the extinction spectra of gold nanoparticles (Figure S9) suspended in the same cell culture media (PBS, DMEM, 10 % FCS in DMEM) as also discussed by Brewer *et al.*[23]

DLS experiments with FCS in water at different concentrations confirmed the stabilizing effect of FCS in DMEM also for lower protein concentrations (Figure S8A). We also followed the time course of the stability of the nanoparticles. Accordingly, the particles remained stable at least for 24 hours in FCS-containing media (Figure S8B). Similarly, we observed that induced aggregation by sodium chloride (aggregation occurs as a consequence of electostatic destabilization) could be slowed down significantly in 10 % FCS in DMEM indicating the formation of a stabilizing biomolecule corona. The stability of primary silver nanoparticles as well as gold nanoparticles under the incubation conditions confirms that their

entry into the cell occurs by endocytosis of individual nanoparticles or of very small aggregates.[24-27] This is confirmed by X-ray microscopy, showing many separated single nanoparticles in the cytoplasm of fibroblast cells after 3 hours of incubation in good agreement with the DLS data showing primary particles in the incubation medium.

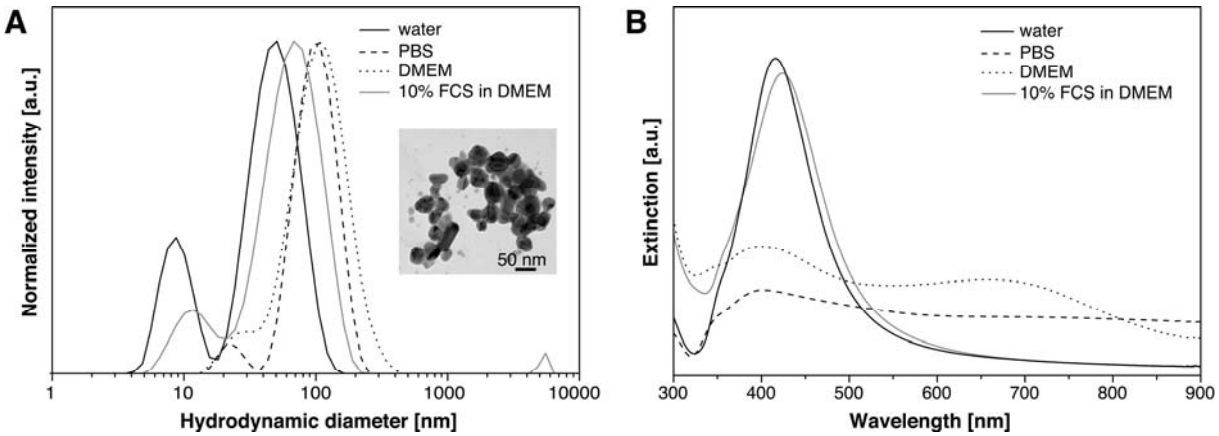

Figure S7. Particle size distribution (**A**) and extinction spectra (**B**) of citrate-stabilized silver nanoparticles in cell culture relevant media.

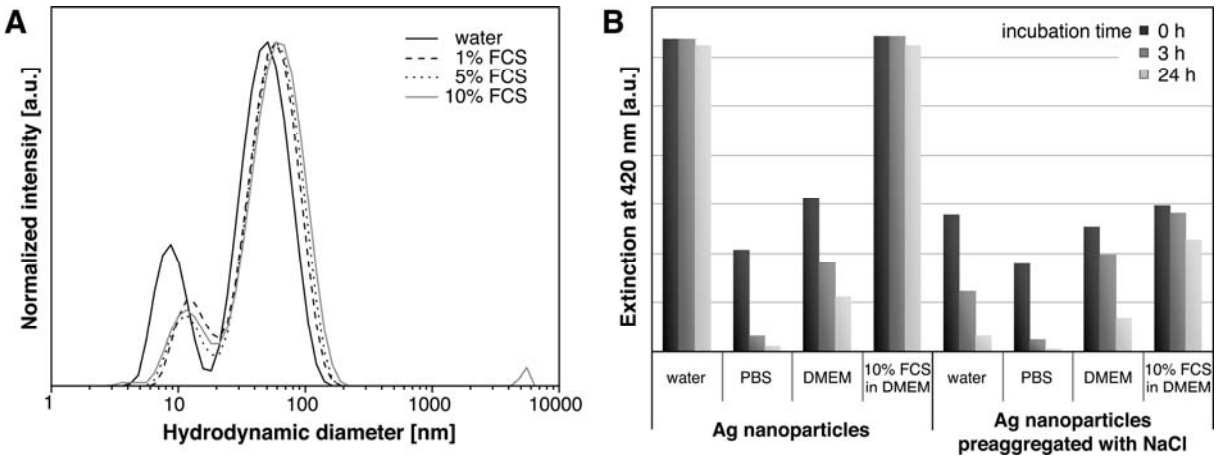

Figure S8. (**A**) Particle size distribution of citrate-stabilized silver nanoparticles in 1 %, 5 % and 10 % FCS in water. (**B**) Extinction at 420 nm of Ag nanoparticles in different cell culture relevant media. This extinction maximum is typical of localized surface plasmons of isolated silver nanoparticles with extinction decreasing in the process of particle aggregation (compare Figure S7B).

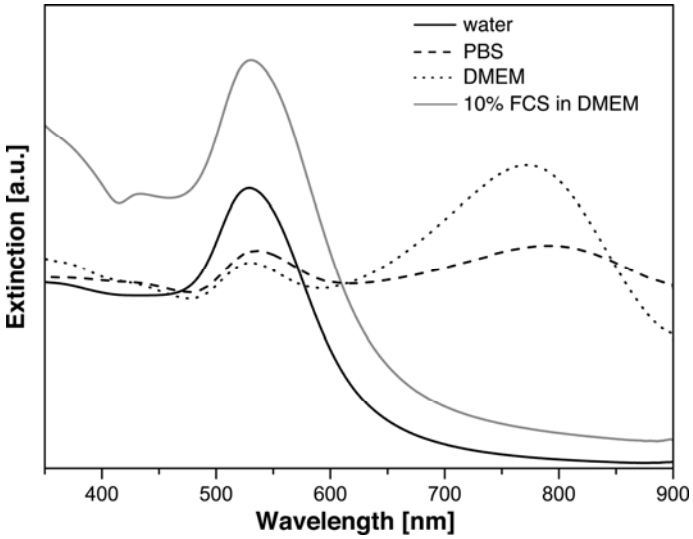

Figure S9. Extinction spectra of citrate-stabilized gold nanoparticles in cell culture relevant media.

Distribution of the silver nanoparticles in the cells

The intracellular distribution of silver nanoparticles in 3T3 fibroblast cells can be followed and mapped using the SERS signal from the corona (Figure S10). The intensity of the C-S stretching vibration of cysteine at 658 cm^{-1} was used for SERS chemical imaging. As illustrated in Figure 10A the coated silver nanoparticles are homogeneously distributed in the cytoplasm after 3 hours of incubation. With increasing incubation time the silver nanoparticles accumulated in the proximity of the nucleus (Figure 10B). Even though the smaller nanoparticles contained in the broad size distribution could in principle pass the nuclear pores, this was not observed. This would require an escape from the endosomal system.[28, 29]

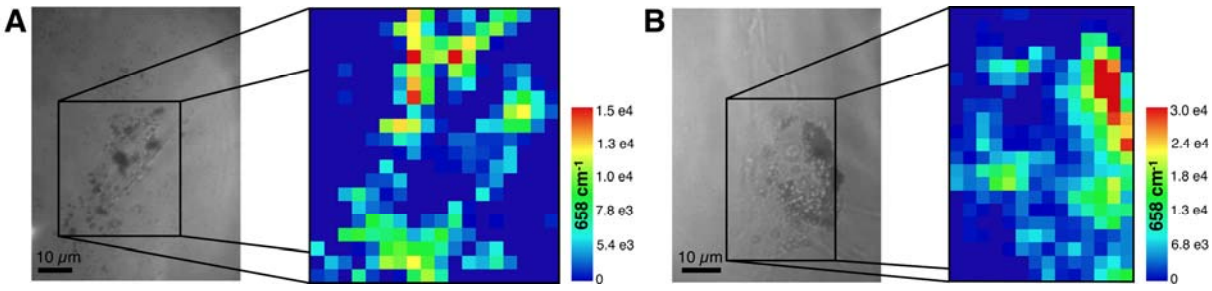

Figure S10. Bright field images and SERS chemical images of 3T3 fibroblast cells incubated with Ag nanoparticles (100 pM) for 3 hours (**A**) and 24 hours (**B**). The chemical images were generated based on the intensity of the C-S stretching vibration at 658 cm^{-1}.

Table S1. Band assignments (tentative) for the SERS spectra of 3T3 cells, fetal calf serum (FCS), Dulbecco's Modified Eagle Medium (DMEM), and cysteine displayed in Figure 3. Assignments are based on references.[21, 22, 30-32]

Raman shift In cm^{-1}	**Assignments**	**3T3 cells**	**FCS**	**DMEM**	**Cysteine**
524	ν(S-S)			x	
598		x		x	
625	$\gamma_W(COO^-)$, γ_T(C-C)		x		
658	$\nu(C\text{-}S)_{trans}$	x	x	x	x
722	$\delta(COO^-)$	x	x	x	
734	$\nu(C\text{-}S)_{gauche}$	x		x	x
760	Trp			x	
800					x
895	ν(C-C)				x
910	ν(C-C)	x		x	x
967	ν(C-C)	x	x	x	
1096	$\rho(NH_2)$, ν(C-N)		x		
1134-1152	$\delta(NH_3^+)$	x	x	x	
1246	Amide III, $\gamma_W(CH_2)$		x		
1288	$\gamma_W(CH_2)$	x		x	x
1331	δ(CH), $\gamma_W(CH_2)$		x		
1376				x	
1456	CH_2 sciss, $\delta_{as}(CH_3)$		x	x	
1587	ν(ring CC), $\nu_{as}(COO^-)$		x		
1600-1625	ν(C=O)	x		x	

*Abbreviations: ν, stretching; δ, deformation; ρ, rocking; γ_T, twisting; γ_W, wagging; as, asymmetrical; Trp, tryptophan.

REFERENCES

1. D. Drescher; G. Orts-Gil; G. Laube; K. Natte; R. W. Veh; W. Österle; J. Kneipp, *Analytical and Bioanalytical Chemistry,* 2011, **400** (5), 1367.
2. D. Weiß; G. Schneider; B. Niemann; P. Guttmann; D. Rudolph; G. Schmahl, *Ultramicroscopy,* 2000, **84** (3-4), 185.
3. G. Schneider; E. Anderson; S. Vogt; C. Knöchel; D. Weiss; M. Legros; C. Larabell, *Surface Review and Letters,* 2002, **9** (1), 177.
4. B. L. Henke; E. M. Gullikson; J. C. Davis, *Atomic Data and Nuclear Data Tables,* 1993, **54** (2), 181.
5. S. Kapishnikov; A. Weiner; E. Shimoni; P. Guttmann; G. Schneider; N. Dahan-Pasternak; R. Dzikowski; L. Leiserowitz; M. Elbaum, *Proceedings of the National Academy of Sciences of the United States of America,* 2012, **109** (28), 11188.
6. W. G. Müller; J. B. Heymann; K. Nagashima; P. Guttmann; S. Werner; S. Rehbein; G. Schneider; J. G. McNally, *Journal of Structural Biology,* 2012, **177** (2), 179.
7. G. Schneider; P. Guttmann; S. Heim; S. Rehbein; F. Mueller; K. Nagashima; J. B. Heymann; W. G. Müller; J. G. McNally, *Nature Methods,* 2010, **7** (12), 985.
8. S. Arora; J. Jain; J. M. Rajwade; K. M. Paknikar, *Toxicology Letters,* 2008, **179** (2), 93.
9. S. M. Hussain; K. L. Hess; J. M. Gearhart; K. T. Geiss; J. J. Schlager, *Toxicology In Vitro,* 2005, **19** (7), 975.
10. R. F. Aroca; R. A. Alvarez-Puebla; N. Pieczonka; S. Sanchez-Cortez; J. V. Garcia-Ramos, *Advances in Colloid and Interface Science,* 2005, **116** (1-3), 45.
11. A. K. Campion, P., *Chemical Society Reviews,* 1998, **27** (4), 241.
12. M. Moskovits, *Reviews of Modern Physics,* 1985, **57**, 783.
13. Y. W. C. Cao; R. C. Jin; C. A. Mirkin, *Science,* 2002, **297** (5586), 1536.
14. N. F. L. Machado; C. Ruano; J. L. Castro; M. P. M. Marques; J. C. Otero, *Physical Chemistry Chemical Physics,* 2011, **13** (3), 1012.
15. B. D. Moore; L. Stevenson; A. Watt; S. Flitsch; N. J. Turner; C. Cassidy; D. Graham, *Nature Biotechnology,* 2004, **22** (9), 1133.
16. J. Ando; K. Fujita; N. I. Smith; S. Kawata, *Nano Letters,* 2011, **11** (12), 5344.
17. J. Kneipp; H. Kneipp; B. Wittig; K. Kneipp, *Nano Letters,* 2007, **7**, 2819.
18. A. K. Oyelere; P. C. Chen; X. Huang; I. H. El-Sayed; M. A. El-Sayed, *Bioconjugate Chemistry,* 2007, **18** (5), 1490.

19. J. M. Yuen; N. C. Shah; J. T. Walsh, Jr.; M. R. Glucksberg; R. P. Van Duyne, *Analytical Chemistry,* 2010, **82** (20), 8382.

20. J. Kneipp; H. Kneipp; K. Kneipp, *Proceedings of the National Academy of Sciences of the United States of America,* 2006, **103** (46), 17149.

21. J. Kneipp; H. Kneipp; M. McLaughlin; D. Brown; K. Kneipp, *Nano Letters,* 2006, **6** (10), 2225.

22. J. Kneipp; H. Kneipp; A. Rajaduraj; R. W. Redmond; K. Kneipp, *Journal of Raman Spectroscopy,* 2009, **40**, 1.

23. S. H. Brewer; W. R. Glomm; M. C. Johnson; M. K. Knag; S. Franzen, *Langmuir,* 2005, **21** (20), 9303.

24. B. D. Chithrani; J. Stewart; C. Allen; D. A. Jaffray, *Nanomedicine,* 2009, **5** (2), 118.

25. C. Greulich; J. Diendorf; T. Simon; G. Eggeler; M. Epple; M. Köller, *Acta Biomaterialia,* 2011, **7** (1), 347.

26. P. Nativo; I. A. Prior; M. Brust, *ACS Nano,* 2008, **2** (8), 1639.

27. N. M. S. Sirimuthu; C. D. Syme; J. M. Cooper, *Analytical Chemistry,* 2010, **82** (17), 7369.

28. E. Oh; J. B. Delehanty; K. E. Sapsford; K. Susumu; R. Goswami; J. B. Blanco-Canosa; P. E. Dawson; J. Granek; M. Shoff; Q. Zhang; P. L. Goering; A. Huston; I. L. Medintz, *ACS Nano,* 2011, **5** (8), 6434.

29. J. A. Ryan; K. W. Overton; M. E. Speight; C. M. Oldenburg; L. Loo; W. Robarge; S. Franzen; D. L. Feldheim, *Analytical Chemistry,* 2007, **79** (23), 9150.

30. A. Kudelski; W. Hill, *Langmuir,* 1999, **15** (9), 3162.

31. S. Stewart; P. M. Fredericks, *Spectrochimica Acta A,* 1999, **55** (7-8), 1641.

32. H. Sugeta; A. Go, *Chemistry Letters,* 1972, (1), 83.